International Journal of Geo-Information

MDPI

Article

Saline-Soil Deformation Extraction Based on an Improved Time-Series InSAR Approach

Wei Xiang [1], Rui Zhang [1,2,*], Guoxiang Liu [1,2], Xiaowen Wang [1], Wenfei Mao [1], Bo Zhang [1], Yin Fu [1] and Tingting Wu [1]

[1] Faculty of Geosciences and Environmental Engineering, Southwest Jiaotong University, Chengdu 610031, China; xiangwei@my.swjtu.edu.cn (W.X.); rsgxliu@swjtu.edu.cn (G.L.); insarwxw@swjtu.edu.cn (X.W.); wenfeimao@my.swjtu.edu.cn (W.M.); rsbozh@my.swjtu.edu.cn (B.Z.); rsyinfu@my.swjtu.edu.cn (Y.F.); wutingting@my.swjtu.edu.cn (T.W.)

[2] State-Province Joint Engineering Laboratory of Spatial Information Technology of High-Speed Rail Safety, Southwest Jiaotong University, Chengdu 610031, China

* Correspondence: zhangrui@swjtu.edu.cn; Tel.: +86-13568813182

Abstract: Significant seasonal fluctuations could occur in the regional scattering characteristics and surface deformation of saline soil, and cause decorrelation, which limits the application of the conventional time-series InSAR (TS-InSAR). For extending the saline-soil deformation monitoring capability, this paper presents an improved TS-InSAR approach, based on the interferometric coherence statistics and high-coherence interferogram refinement. By constructing a network of the refined interferograms, high-accuracy ground deformation can be extracted through the weighted least square estimation and the coherent target refinement. To extract the high-accuracy deformation of a representative saline soil area in the Qarhan Salt Lake, 119 C-band Sentinel-1A images collected between May 2015 and May 2020 are selected as the data source. Subsequently, 845 refined interferograms are selected from all possible interferograms to conduct the network inversion, based on the related thresholds (the temporal baseline <49 days, the average spatial coherences >0.5, respectively). Compared with the conventional TS-InSAR measurements, both the accuracy and reliability of the extracted deformation results of the saline soil increased dramatically. Furthermore, the testing results indicate that the improved TS-InSAR method has advantages on the deformation extraction in the saline soil region, and is adaptive to reflecting the typical seasonal variations of the saline soil.

Keywords: saline soil; ground deformation; Qarhan Salt Lake; coherence analysis; time-series InSAR

Citation: Xiang, W.; Zhang, R.; Liu, G.; Wang, X.; Mao, W.; Zhang, B.; Fu, Y.; Wu, T. Saline-Soil Deformation Extraction Based on an Improved Time-Series InSAR Approach. *ISPRS Int. J. Geo-Inf.* **2021**, *10*, 112. https://doi.org/10.3390/ijgi10030112

Academic Editor: Wolfgang Kainz

Received: 26 December 2020
Accepted: 24 February 2021
Published: 27 February 2021

1. Introduction

Interferometric Synthetic Aperture Radar (InSAR) is an emerging and valuable technique for ground deformation monitoring [1,2]. This spaceborne observation technique can monitor surface changes for a large area with millimeter-level precision and meter-level resolution [3]. However, due to the changes of signal propagation and scattering properties, the conventional InSAR measurements are affected by systematic and random errors, e.g., inaccurate satellite orbit, atmospheric delays, surface elevation bias, and surface scatterers variations. The resulting spatiotemporal decorrelation would degrade the deformation accuracy of InSAR [4–6], and this problem would even cause failed extraction of ground deformation [7–9]. It should be noted that InSAR is a differential method, so all the measurements produced are relative observations both in space and time [10]. Therefore, a relatively stable reference point is needed, but its constant movements cannot be recognized, such as crustal movements that occur over large areas, and the accuracies of low wave number components of the velocity field decrease with increasing distance from them [11].

To compensate for the deficiencies of InSAR listed above, time-series InSAR (TS-InSAR) techniques utilize the sequential SAR images to extract the ground deformation [12–14].

There are two main approaches of TS-InSAR. The first category, named persistent scatterer (PS) InSAR, concentrates on the pixels with temporal scattering steadiness and extracts the time series deformation of the identified pixels based on their phase variation in the spatiotemporal domain [9,15]. Such methods are dedicated to tracking the deformation of phase-stable scatterers, and have been successfully applied to urban areas [16,17], whereas in non-urban areas, especially vegetated areas and desert areas, it is hard to find enough PSs for the regional deformation extraction. Nevertheless, the second category named small-baseline subset (SBAS) InSAR, estimates the ground deformation by using the interferograms with short spatiotemporal baselines [18,19]. Such a method is designed to maximize the interferometric coherence for more distributed targets [20,21]. Consequently, the ground deformation of each high-coherence object can be extracted. The SBAS technique has been successfully applied to the time-series deformation monitoring for landslide, volcanic, permafrost, etc. [22,23].

However, the spatiotemporal baseline of the conventional SBAS-InSAR technique is constrained in a certain threshold, which may only induce a few interferograms for the deformation calculating. Especially in saline soil areas, significant seasonal fluctuations of the scattering characteristics and ground deformation [24] may bring about many unpredictable errors (e.g., temporal decorrelation, unwrapping errors, etc.) in some interferograms. Therefore, the redundant observations result from the conventional SBAS-InSAR technique are not enough to make sure the accuracy and reliability of the estimated deformation velocity, and it may lead to the lack of phase consistency [25]. Because of the continuous propagation of noises, the lack of phase consistency and low-quality interferograms may also reduce the accuracy and the reliability of the time-series deformation.

Some good interferogram network refinement strategies have been used for reducing the phase errors and enhancing the co-registration accuracy, especially those algorithms based on graph theory [26], and sequential network [27]. In order to reduce the influence of the unpredictable errors on the deformation results, we analyze the interferometric coherences in a longer temporal baseline and optimize the interferogram stacks for a better quality of the observations. By using the interferogram stacks with high coherence, an improved network of interferograms without temporal baseline constraints presented in this paper can mitigate the statistical noises of the estimated time-series deformation. Moreover, such an improved method can also provide a good choice for high-quality interferogram selection and deformation extraction in the areas with significant seasonal fluctuations (such as permafrost, glacier). The main procedures of such an improved TS-InSAR are presented in the following sections, including interferogram networking and network inversion by the weighted least square (WLS) estimator. To test the improved TS-InSAR method in a typical saline soil area, 119 Sentinel-1A images acquired over Qarhan Salt Lake between 21 May 2015 and 18 May 2020 are applied to construct the interferogram network and subsequent network inversion for time-series deformation extraction. Above all, the average spatial coherence (ASC) of 2921 interferograms formed by the Sentinel-1A images with the perpendicular baseline of 200 meters and the temporal baseline of 400 days are calculated. Subsequently, there are 392 interferograms selected for the conventional SBAS-InSAR with the appropriate temporal baseline of 49 days after analyzing the coherences of the interferograms. Ultimately, the 845 interferograms with ASC more than 0.5 are selected to conduct the network inversion by the WLS estimator.

2. Methodology

In salt deserts the interferometric coherence may mainly be affected by soil moisture and surface water. The seasonal precipitation is the main external environmental factor that influences soil moisture and surface water [28]. Therefore, the temporal decorrelation and seasonal deformation may be the distinct characteristics in the saline soil areas. In addition, since the spatial baseline of Sentinel-1A is accurately controlled within 200 m, the topographic error by a long spatial baseline can be neglected [29]. Consequently, the temporal baseline is the main concern that may cause decorrelation.

For accurately monitoring the ground deformation in the saline soil area, the improved TS-InSAR method presented in this paper is focused on the interferogram selection with high coherence. There is no temporal baseline constraint and only a concern about the interferometric coherence for the interferogram networking and the coherent target (CT) selection. Since the CTs are selected by multi-constrained interferometric coherences, i.e., spatial coherence (SC) threshold for differential InSAR (DInSAR) processing, the average spatial coherence (ASC) threshold for the interferogram selection, the temporal coherence threshold for the CT selection [30], the final amount of the refined CTs are relatively scarce. Therefore, ensuring the abundant CTs with high reliability is the key point for the time-series deformation monitoring.

To acquire abundant deformation measurements in the saline soil area, an appropriate interferogram network is proposed in this section. The improved TS-InSAR procedures including interferometric coherence analysis, interferogram networking, network inversion and the CT selection, are described in detail. The data processing flow adopted in this paper is shown in Figure 1. It should be noted that, all the interferograms are unwrapped by the minimum cost flow (MCF) method before the interferogram network inversion.

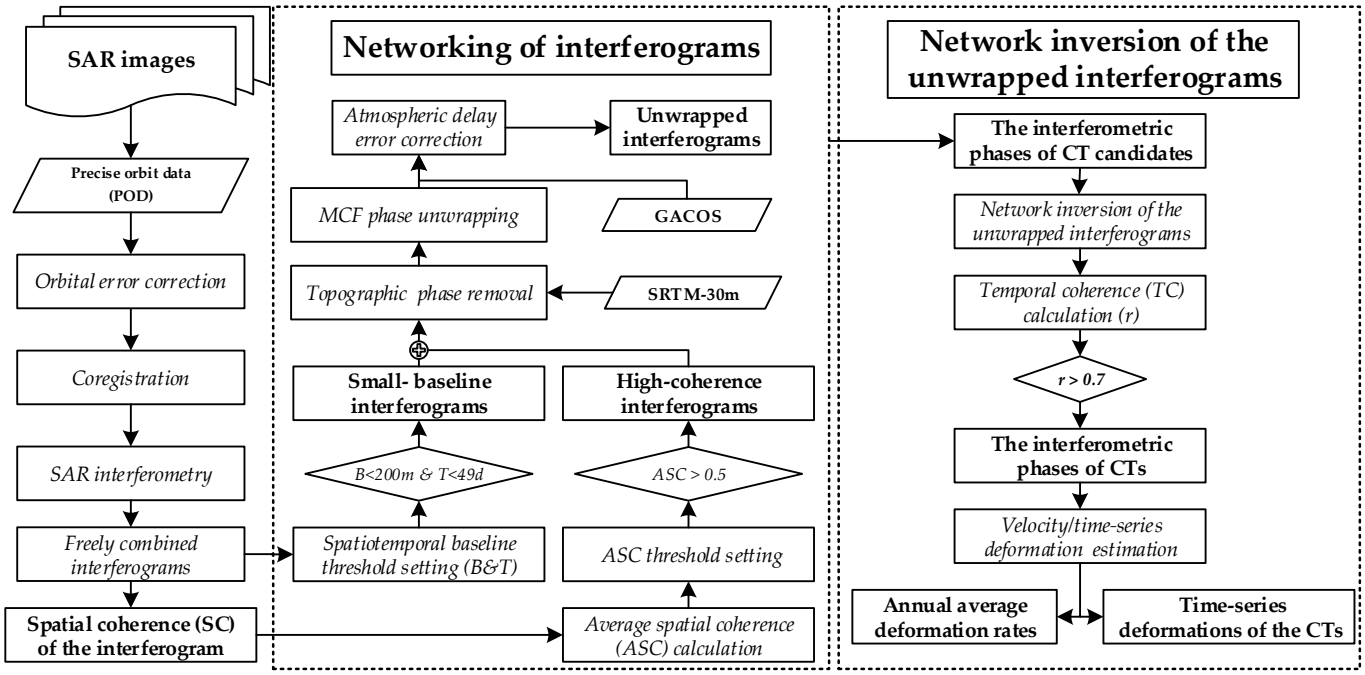

Figure 1. The processing flow of the improved TS-InSAR, *B* and *T* indicate perpendicular baseline and temporal baseline, respectively.

2.1. Interferometric Coherence Analysis

Actually, the deformation measurement of DInSAR is a process of converting the phase difference into deformation by measuring the phase difference between radar waves. The phase difference indicates the spatial geometry information, which represents the displacement of the SAR line of sight (LOS) direction. However, the phase difference contains a series of error terms in addition to the actual deformation, e.g., inaccurate satellite orbit, atmospheric delay, surface elevation bias, surface scatterers variation. The SC coefficient is usually used to evaluate the quality of the phase difference derived by the interferometry between two SAR images. Therefore, in order to extract the deformations of

high quality CTs, it is necessary to measure the SC, firstly. The calculation model of the SC coefficient can be expressed by the following equation [21]:

$$\gamma_{spt} = \frac{\sum_{n=1}^{R}\sum_{m=1}^{C} u_1(n,m)u_2{}^*(n,m)}{\sqrt{\sum_{n=1}^{R}\sum_{m=1}^{C}|u_1(n,m)|^2\sum_{n=1}^{R}\sum_{m=1}^{C}|u_2(n,m)|^2}} \quad (1)$$

where * represents complex conjugate, $u_1(n,m)$ and $u_2(n,m)$ represent the complex values at (n,m) which is the image coordinate in the primary and secondary image data blocks, $|u_1(n,m)|^2$ represents the second-order norm of the data, R and C represent the size of the data block for calculating the coherence, n and m are the row and column numbers in the data block, then it takes any pixel as the center and calculates the coherence coefficients according to the window size of $n \times m$. The coherence coefficient of any pixel is used as an indicator to evaluate the quality of the interferometric phase of such pixel [8].

The ASC is an indicator of the interferometric quality for each interferogram, and also reflects the variation of ground scattering characteristics. The ASC of all the pixels in the interferogram can be represented by:

$$\gamma_{asc} = \frac{\sum_{i=1}^{S}\gamma_{spt}^{i}}{S} \quad (2)$$

where S is the number of all pixels in the interferogram.

There are three kinds of coherences in this paper, i.e. SC, ASC, and TC. Firstly, the SC of each pixel is used to evaluate the quality of the interferometric phase, and any pixel conforming to the preset threshold can be selected as a CT by DInSAR processing. Then the ASC of any interferogram which is higher than a preset threshold can be participated in the construction of interferogram network. Subsequently, the interferogram network inversion can be conducted by using the WLS estimator, and the TC can be used to select high-quality CTs. Finally, the time series deformations of CTs in the study area can be obtained. TC can be expressed by [31]:

$$\gamma_{temp} = \frac{1}{M}\left|\sum_{i=1}^{M}\exp[j(\Delta\varphi_i - A\hat{=}\varphi_i)]\right| \quad (3)$$

where j is the imaginary unit, M is the number of differential interferograms, $\Delta = \varphi_i$ is the interferometric phase of each interferogram, $\hat{=}\varphi_i$ is the best estimation of time series interferometric phase, A is a design matrix which represents the interferometric combination mode. The detailed information of the above variables will be described in the subsequent sections.

2.2. High Coherence Interferogram networking

Assuming that there are $N + 1$ SAR images covering the same area in the time series of $t = [t_0, \ldots, t_N]^T$, M differential interferograms can be obtained, then:

$$\frac{N+1}{2} \le M \le N\left(\frac{N+1}{2}\right) \quad (4)$$

However, the combination of image pairs plays a crucial role in TS-InSAR monitoring. On the one hand, if each image acquired date is only connected to the adjacent image date (see the CASE 0 in Figure 2), there is no redundant observation and the estimated result may be inaccurate. On the other hand, if all interferograms are freely combined, there will be $(N+1)N/2$ interferograms from $N + 1$ images. This combination strategy of freely connected network increases a large number of redundant observations, which can be applicable to a research area with low coherence. Nevertheless, the huge amount of interferograms will greatly reduce the computing efficiency. Moreover, the low-quality interferograms will affect the accuracy of time-series results.

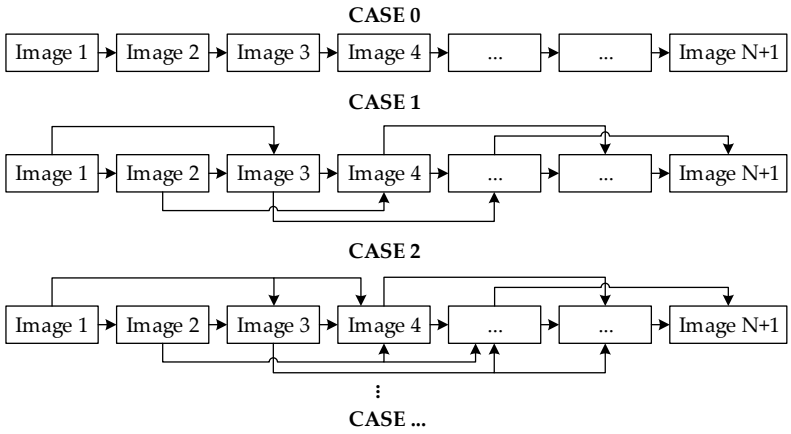

Figure 2. The interferogram networking categories for N + 1 SAR images.

In the conventional SBAS-InSAR method, one of the images is selected as the primary image for the coregistration, and the interferometric pairs conforming to the spatiotemporal baseline threshold are selected from all the freely combined interferograms. The interferograms with a small baseline can be applied to the situation with rapid decorrelation in the time domain. However, the SBAS-InSAR method constrains the spatiotemporal baseline and rejects other high-quality interferograms. Consequently, there may be no redundant observation for some isolated interferograms, and such category may induce the accumulated error propagation. To limit the propagation of errors, high-quality redundant observations can be added to network of interferograms. In such a case, there is no spatiotemporal baseline threshold constraint, and all the interferograms that are conforming to the ASC threshold can be participated in the interferogram networking.

2.3. Interferogram Network Inversion by WLS Estimator

The interferometric phase of each interferogram is composed of multiple phase components and can be presented by:

$$\psi = \varphi_{\text{ref}} + \varphi_{\text{top}} + \varphi_{\text{def}} + \varphi_{\text{atm}} + \varphi_{\text{noi}} \tag{5}$$

where, ψ represents the interferometric phase generated by the interferometric image pair; φ_{ref} is the phase of the reference ellipsoid; φ_{top} is the topographic phase caused by terrain undulation; φ_{def} is the LOS deformation phase caused by surface displacement during the two imaging periods of the satellite; φ_{atm} is the delay phase caused by the inconsistency of atmospheric state at the two acquisitions time; φ_{noi} is random noise. After flat-earth phase removal, topographical phase removal and interferometric phase unwrapping, the interferometric phase of each interferogram can be expressed as [32]:

$$\Delta\varphi = A\varphi + \Delta\varphi_{\varepsilon} \tag{6}$$

where, $\Delta\varphi = \left[\Delta\varphi^1, \ldots, \Delta\varphi^M\right]^T$ is the interferometric phase of each interferogram; $\varphi = \left[\varphi^1, \ldots, \varphi^N\right]^T$ is the temporal interferometric phase of other images relative to the reference image (assuming that the acquisition time of the reference image is t_0), $\Delta\varphi_{\varepsilon} = \left[\Delta{\varphi_{\varepsilon}}^1, \ldots, \Delta{\varphi_{\varepsilon}}^M\right]^T$ is the residual interferometric phase error, and A is a M $\times$ N design matrix which represents the interferometric combination mode and consists of 1, 0, and -1, where -1 represents the master image and 1 represents the slave image. The least square norm method can be used to calculate the optimal estimation value of time series interferometric phase [30,33]:

$$\hat{\varphi} = \text{argmin}\|W^{1/2}(\Delta\varphi - A\varphi)\|_2 = \left(A^T W A\right)^{-1} A^T W \Delta\varphi \tag{7}$$

where, $\hat{\varphi}$ is the best estimation of time series interferometric phase, W is a $M \times M$ diagonal weight matrix, and the weight Matrix method adopted in this paper is Fisher Information Matrix (FIM) [34,35], which is expressed as follows:

$$W = diag\left\{\frac{2L\gamma^{1^2}}{1-\gamma^{1^2}}, \ldots, \frac{2L\gamma^{M^2}}{1-\gamma^{M^2}}\right\} \quad (8)$$

where L is the independent multi-look coefficient used to calculate the coherence coefficient. For example, the multi-look coefficient of sentinel-1A radar image is usually set as (10, 2), then $L = 20$. γ can be calculated by formula (1) and is called Spatial Coherence (SC) [21]. The time-series interferometric phase of each CT that conforming to the SC threshold can be obtained by WLS estimation of the interferogram network.

3. Study Area and Data Source

Qaidam Basin is located in the northern section of the Qinghai-Tibet Plateau (QTP) in China. A large number of salt lakes are distributed in this closed inland basin, which is surrounded by the Altun Mountains in the northwest, Qilian Mountains in the northeast and Kunlun Mountains in the south [36]. As shown in Figure 3, Dabuxun Salt Lake, Xiezuo Lake and Tuanjie Lake are the three subparts of Qarhan Salt Lake, located in the southeast of the Qaidam Basin [37,38].

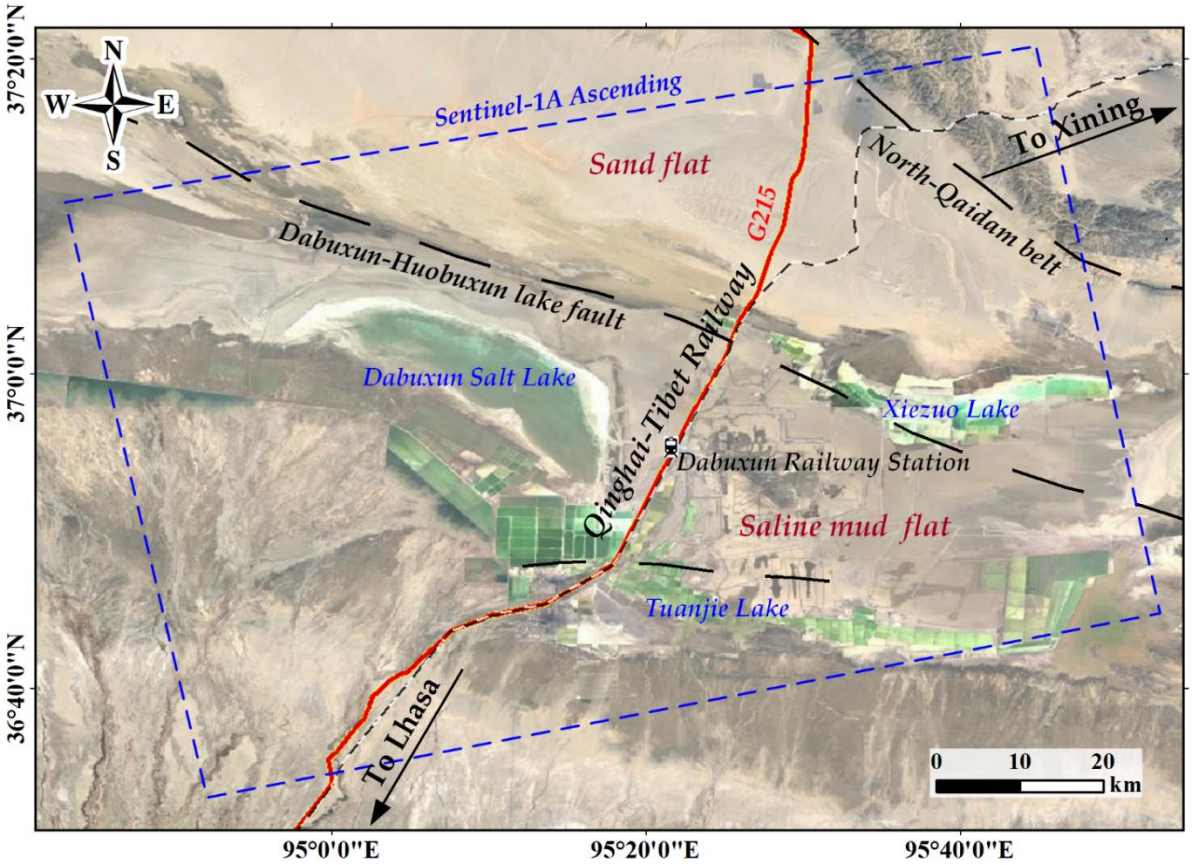

Figure 3. The geographical environment and transportation system in the study area, the black dotted lines indicate the faults, the sand flat and the saline mud flat in the blue dotted rectangle is the study area.

Affected by the inland plateau desert climate, the weather is dry and rainless all year around the Qarhan Salt Lake. According to statistics, the average annual precipitation is only 24 mm (as shown in Figure 4), while the potential evaporation capacity is up to 3564 mm [39]. At present, most of the salt lakes have become dry and saline mud

flats. The saline soil in this region is mainly composed of sedimentary rock salts (NaCl crystals) formed by lake water concentration and salt precipitation. This kind of easily soluble rock salts is characterized by high solubility and fast dissolution [40]. Therefore, the saline soil would collapse caused by precipitation, surface runoffs and salt-lake flooding in summer; while uplift resulted from salt swelling and frost heave in winter. These factors promote the occurrence of engineering geological disasters such as ground collapse, building destruction, road damage. Moreover, the Qarhan Salt Lake is the largest salt mining area in China, and artificial exploitation reduces the amount of high-concentration brine. On the one hand, the confined water intrudes and dissolves the rock salt of the underground soil layer. Consequently, many subsurface salt caves by water erosion come out and result in the collapse of the ground [41,42]. On the other hand, the water discharge and recharge in the underground aquifer may also lead to the subsidence and rebound deformation of the ground. These factors will lead to serious security risks in human infrastructures, such as the Qinghai-Tibet Railway (QTR) and the Beijing-Tibet Expressway crossing the dry saline mud flat in the middle of the salt-lake.

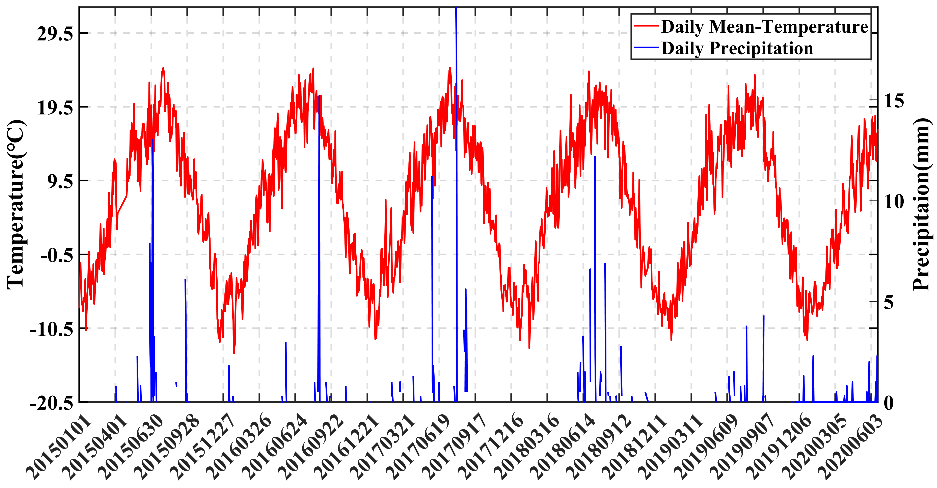

Figure 4. The daily temperature and precipitation data of the Golmud station (36.417° N, 94.9° E) from January 2015 to June 2020.

In order to detect and extract the surface deformation of the Qarhan Salt Lake region, we selected 119 Sentinel-1A C-band (the wave length is 5.6 cm) SAR images with the resolution of 2.33 m × 13.97 m (range × azimuth) from the European Space Agency (ESA). The Sentinel-1 SAR image provides us with high-quality images covering a width of 250 km in the Terrain Observation by Progressive Scans (TOPS) mode, and the revisit time is usually 12 days. All the VV-polarized Sentinel-1A TOPS SAR images collected during 21 May 2015 through 18 May 2020 have already been focused and converted to the Single Look Complex (SLC) format in this paper. The Digital Elevation Model (DEM) data of the study area is generated through the Shuttle Radar Topography Mission (SRTM) with a resolution of 30 m provided by National Aeronautics and Space Administration (NASA). Besides, the Precise Orbit Data (POD) of Sentinel-1A provided by ESA is used to correct the orbital errors, and GACOS data is used to correct the atmospheric delay errors [43,44].

4. Results

4.1. Interferometric Coherence Analysis and Networking of the Interferograms

To optimize the interferometric combinations for a better quality of the interferometric phase, a relatively large temporal baseline threshold is set initially for seeking enough candidate interferograms. In this paper, by setting the temporal baseline threshold for 400 days that includes a whole year and the perpendicular spatial baseline threshold for 200 meters, totally 2921 interferograms are formed with 119 Sentinel-1A images acquired from 2015 to 2020 (by the combination strategy of images in Section 2.2). Then we calculate the average

interferometric coherence coefficients of these 2921 interferograms for further analysis, as shown in the left subplot of Figure 5. As the acquisition time of sentinel-1A images is different in each year, the time coordinate axis is non-uniform. The high interferometric coherences of interferograms mainly appear between June and November (rainy season), then decrease dramatically after November. Subsequently, high interferometric coherences appear again between November and the next June (dry season). Moreover, the seasonal variations of the interferometric coherences are obvious in the saline soil region, and the coherences decrease dramatically due to the increase of precipitation from dry season to rainy season.

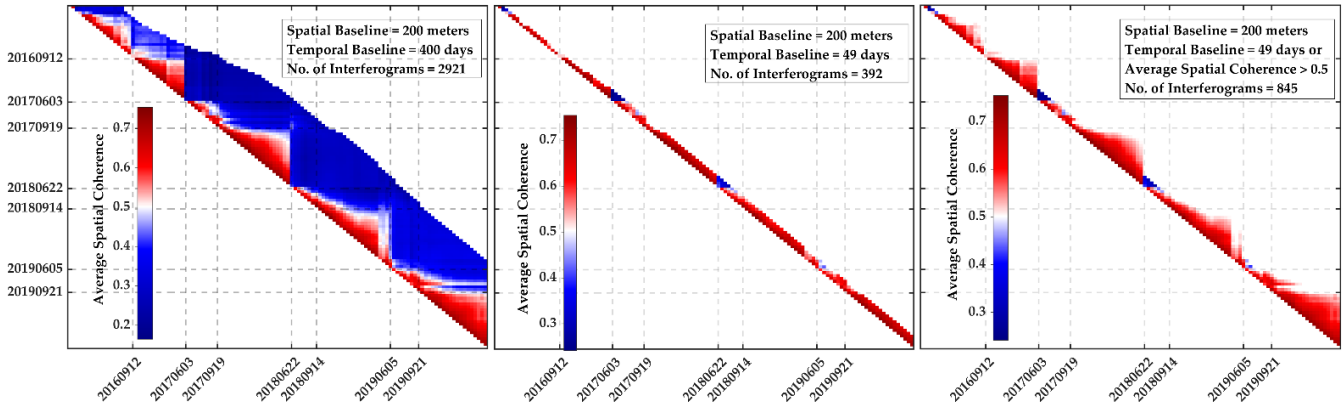

Figure 5. Average interferometric coherence coefficients from 2015 to 2020, The vertical axis represents the time span of the primary images and the horizontal axis represents the time span of the secondary images. The color values of pixels represent the ASC of the interferograms.

There is almost no vegetation cover in the study area, which is bare sandy or mucous saline soil, and the interferometric coherence is high in a short time, as show in Figure 5. High-quality interferometric pairs obtained by temporal baseline threshold are used for forming a interferogram network. Furthermore, in terms of phase consistency, we first set the temporal baseline of 49 days and make sure each SAR image date is combined with at least two others for a better phase closure, which is the same as case 2 in Figure 2. Then the network of a conventional SBAS-InSAR is formed by 392 interferograms, as shown in the middle subplot of Figure 5. However, because of the missing SAR images in some periods, there are still many sequential isolated interferograms for the SBAS-InSAR, this will cause the inaccurate result and accumulated errors propagation in the subsequent calculation procedures.

For making full use of high-coherence interferometric pairs, we add all high-quality interferograms into the network as beneficial redundant observations. As shown in the right subplot of Figure 5, the interferograms with ASC higher than 0.5 are refined as the available interferograms. The number of the interferograms are increased to 845, which means much more redundant observations are participated in the calculation of the network inversion. More valuably, the accumulated errors and the random residues can be mitigated to some extent. As shown in Figure 6, when combining the SAR images by the improved TS-InSAR, the interferogram network is denser during the same season, while sparser between the dry season and the rainy season. Compared to the conventional SBAS-InSAR, there are more high-coherence and redundant interferograms.

4.2. The Deformation Velocity of the Study Area

In this paper, the LOS deformation velocity maps of both the conventional SBAS-InSAR and the improved TS-InSAR are produced under strict processing procedures. The foundations in the geological environment of saline soil and salt lake are very weak and susceptible, and lead to the uneven deformations in the study area, as shown in Figure 7. In the northeastern part of the study area, the deformation velocity maps show that the

ground is stable, while in the middle part, various deformation trends appear including uplift and severe subsidence. The similar deformation characteristics are presented in the southern part.

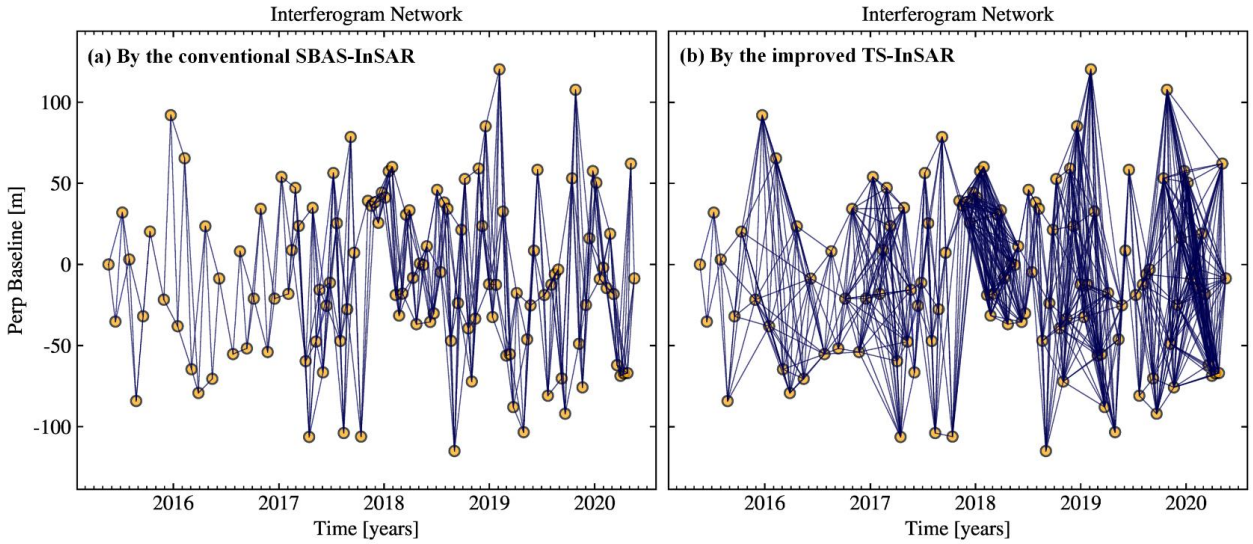

Figure 6. The spatiotemporal baselines of the interferograms for the conventional SBAS-InSAR and the improved TS-InSAR. The time span is from 21 May 2015 to 18 May 2020, and the perpendicular baselines of all the interferograms are between −150 m to 150 m. The threshold of the temporal baseline is 49 days for the conventional SBAS-InSAR, and on that basis, the interferograms with the ASC higher than 0.5 are added in the network for the improved TS-InSAR.

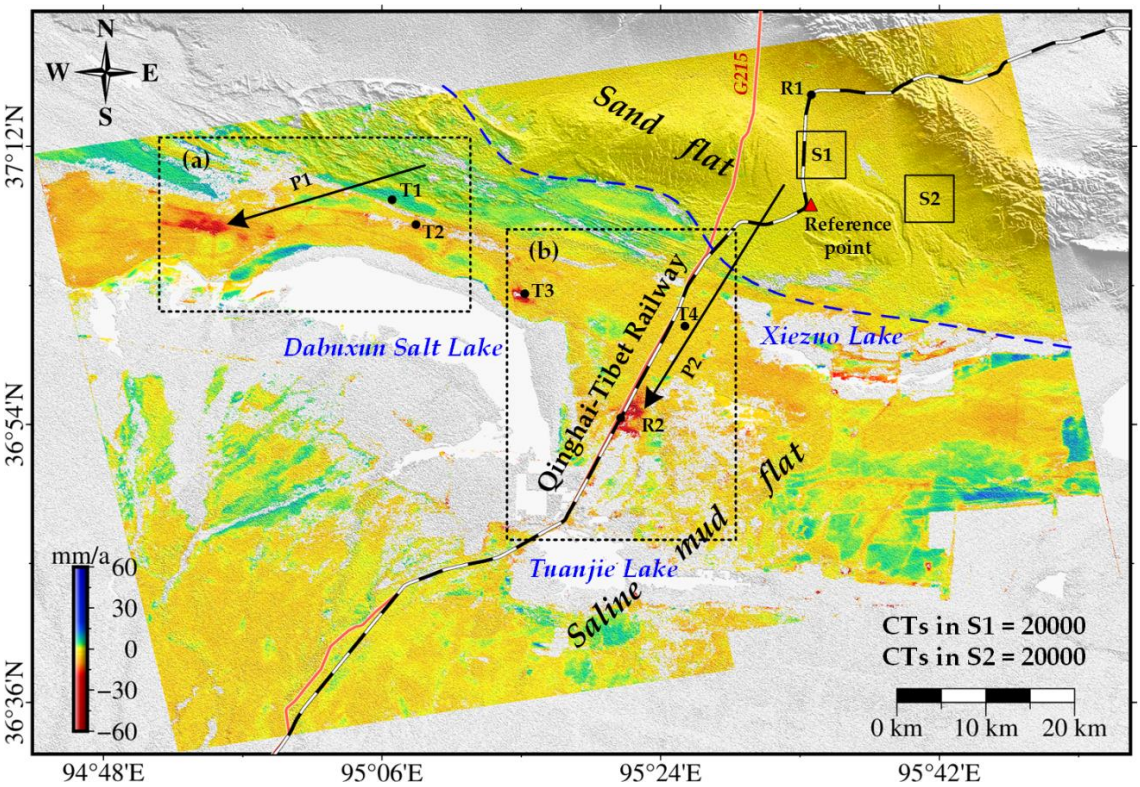

Figure 7. The deformation velocity map derived by the improved TS-InSAR with the temporal baseline of 49 days or ASC of interferograms higher than 0.5. The blue dotted line indicates the boundary between sand flat and saline mud flat, and the red triangle is the reference point with the coordinate 37.1214° N, 95.5346° E. The reference point is selected on an artificial structure of the QTR where is far away from the deformation area affected by the saline soil and the salt lakes.

We plot a dotted blue line in Figure 7 to separate the sand flat and saline mud flat according to the ground deformation velocity and the satellite image. The deformation velocity of sand flat is about 0 mm/a, thus the foundation of it is relatively stable. However, the deformation trends are mostly subsidence in the saline mud flat. There are two significant subsidence areas around points T3 and R2, and both of their maximum deformation velocities are about 60 mm/a in the latest five years. Especially, the subsidence velocity is very significant along the QTR between Dabuxun Salt Lake and Tuanjie Lake, which is dangerous to the safety operation for the railway.

5. Discussion

5.1. Comparison of Different Estimation Strategies

In order to compare the results derived from the conventional SBAS-InSAR and the improved TS-InSAR, we firstly calculate the amounts of CTs for both of them, as shown in Figure 8. The results show that there are 5,842,290 CTs for the conventional SBAS-InSAR, while 5,937,319 CTs for the improved TS-InSAR. There are almost 0.1 million CTs increased by the improved TS-InSAR method. These newly added CTs are distributed in the saline soil area with relatively low coherence or significant seasonal deformation. For example, we select the effective observations in two different kinds of areas for further analyzation, they are A and B respectively. In the area A, as shown in the lower-left subplots of Figure 8, the severe subsidence is mainly caused by the artificial exploitation of brine, and the decorrelation is result from the large gradient deformations. The estimation results of the deformation show that the amount of effective observation points increases in the center of the decorrelation area. In addition, the area B is a natural environmental site, and the deformation of saline soil is influenced by the seasonal change of the surface runoffs, precipitation, etc. The seasonal decorrelation is significant in such a saline soil area. However, the effective observations after the processing of the improved TS-InSAR method are more than that of the conventional SBAS-InSAR.

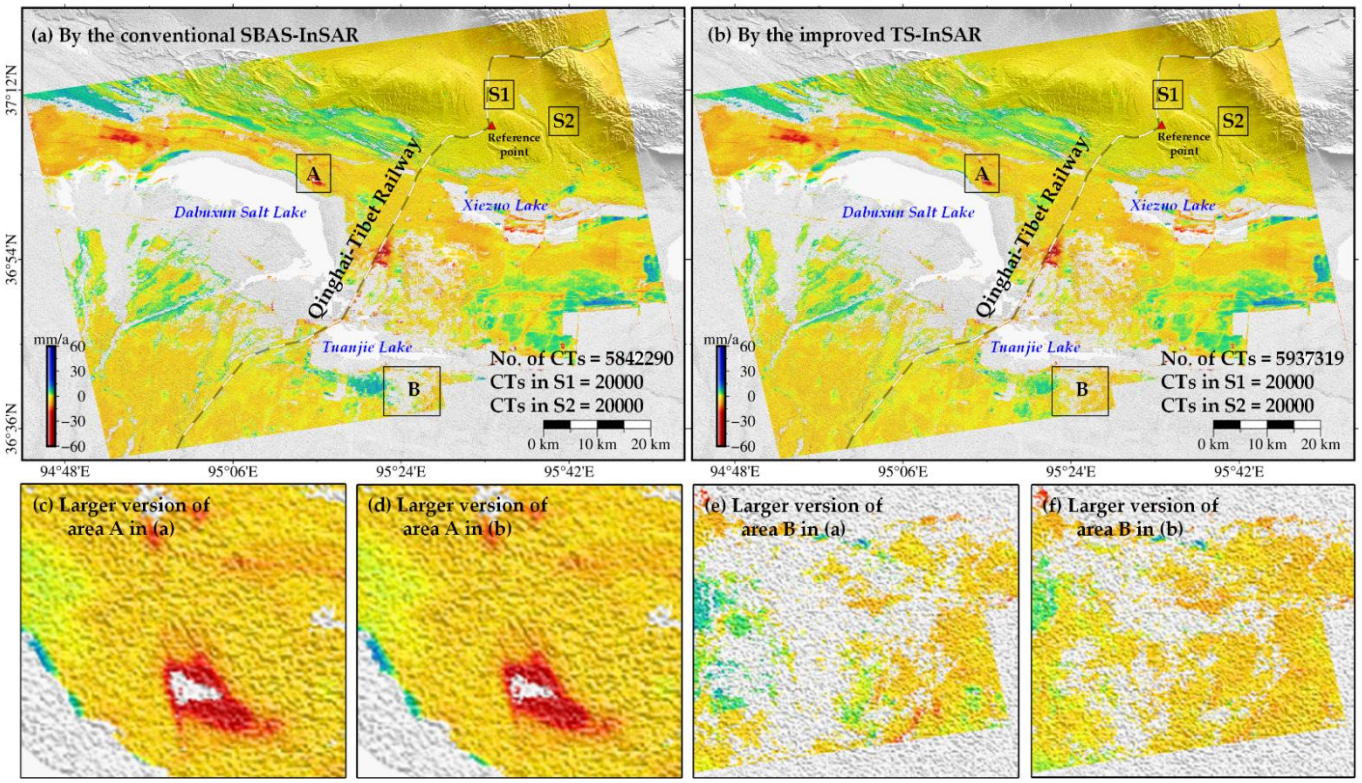

Figure 8. The upper left subplot (**a**) is the deformation velocity map derived by the conventional SBAS-InSAR with the temporal baseline of 49 days, and the upper right subplot (**b**) is the deformation velocity map derived by the improved TS-InSAR with the temporal baseline of 49 days, ASC of interferograms higher than 0.5.

Different estimation strategies could generate the varying accuracy and reliability of the deformation under such a weakened geological environment. Therefore, two relatively stable areas (S1 and S2 in Figure 7) are selected to compare the accuracy and the reliability of the estimated results derived from these two strategies. Both of area S1 and area S2 are with a size of 100 pixels × 200 pixels, and the mean values and the standard deviations of the deformation rates are shown in Figure 9. Especially, we find that both the mean values and the standard deviations of the deformation rates derived from the improved TS-InSAR are smaller than that from the conventional SBAS-InSAR. Furthermore, we count the percentages of the absolute deformation velocity of the conventional SBAS-InSAR and the improved TS-InSAR, respectively. The results show that the absolute deformation velocity smaller than 1.5 mm/a increased from 33% to 79% in area S1, and smaller than 1 mm/a increased from 11% to 67% in area S2. This is mainly due to the improved TS-InSAR with more high-quality redundant observations, which improve the accuracy and reliability of the deformation results in the same seasons, thus limit the error propagation between different seasons and mitigate the residual errors by the adjustment calculation. As a result, such an improved method can enhance the stability of the interferogram network and improve the accuracy and reliability of the inversion results.

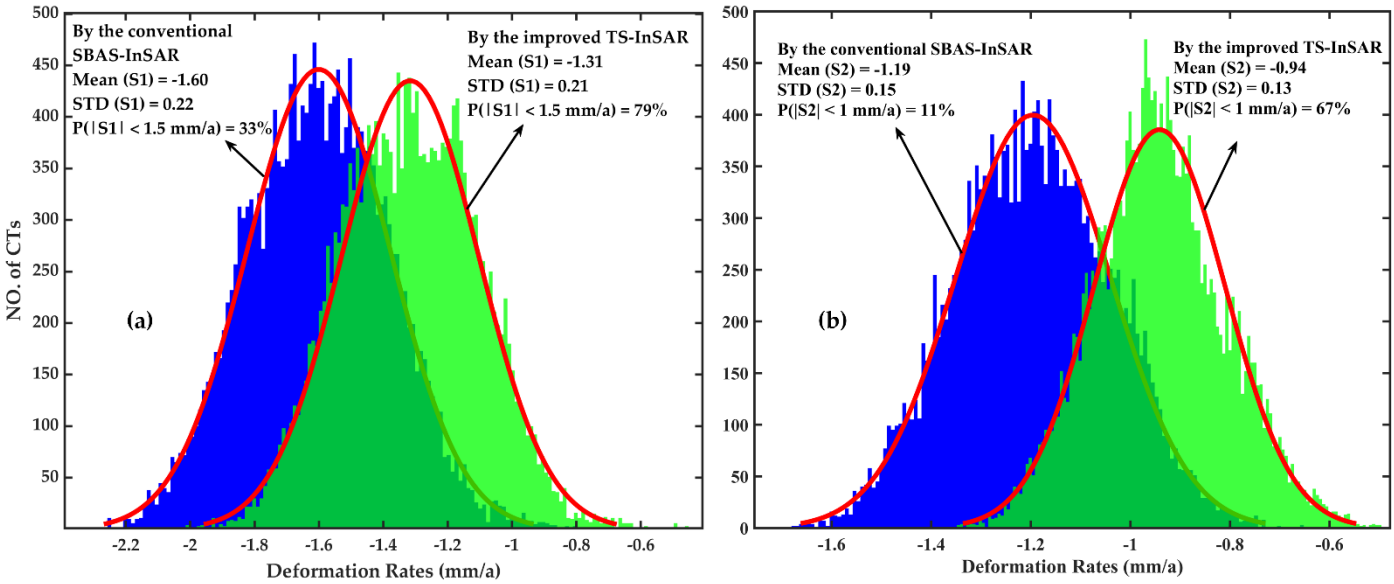

Figure 9. The two subplots are the histogram statistics of the deformation velocity, (**a**) is the results derived by the conventional SBAS-InSAR and the improved TS-InSAR in area S1, respectively, and (**b**) is the results derived by them in area S2.

5.2. The Deformation Characteristics of Areas (a) and (b)

Because of the special geological condition and unstable foundation of saline soil, the safety of the artificial structures attached to the foundation is a matter of concern. According to this issue, areas (a) and (b) in Figure 7 are selected as the representative for analyzing the deformation characteristics of saline soil in the Qaidam Basin. As shown in Figure 7, area (a) is located in the northern part of Dabuxun Salt Lake and the Dabuxun-Huobuxun lake fault (DHLF) is in the middle of it. There are apparently different deformation trends presented in the northern part and the southern part of DHLF, respectively. As shown in Figure 10, the maximum positive LOS velocity which indicates uplift has reached 17 mm/a, and the maximum negative LOS velocity which indicates subsidence has reached −29 mm/a between May 2015 and May 2020.

The opposite deformation trends occur on either side of DHLF, which may be driven by the creep of the compression-shear thrust fault as a previous study suggests [45]. However, the deformation of saline soil is very susceptible to environmental factors, and we thus suspect that the deformation of area (a) should also be driven by the dynamic evolution of

saline soil. To confirm this speculation, we depicted the accumulated deformation maps of area (a) from May 2015 to May 2020, as shown in Figure 11. The seasonal deformation characteristics of saline soil can be observed in some areas, i.e., uplift in the dry seasons from September to the next May, and subsidence in the rainy seasons from May to September.

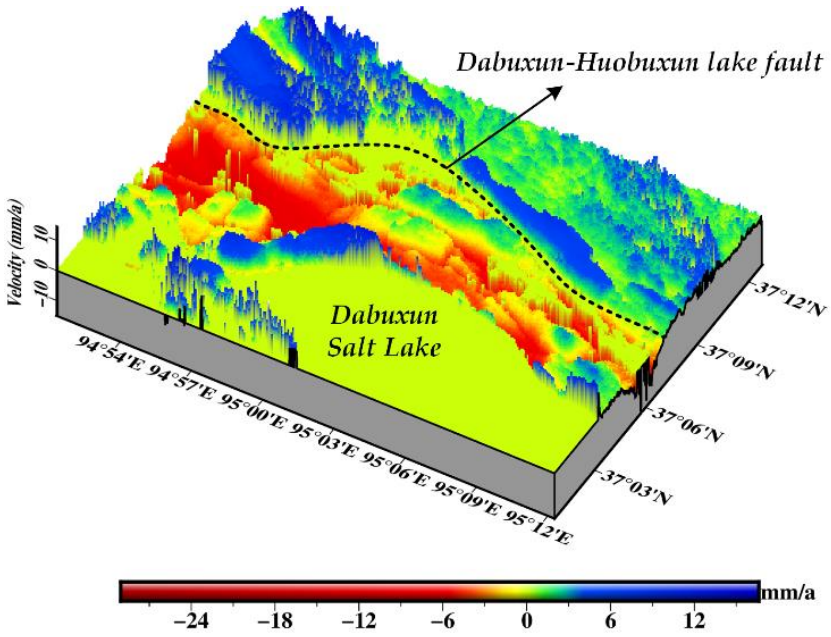

Figure 10. 3D view of the deformation velocity in area (a) which is depicted in Figure 7, the black dotted line in the middle indicates the Dabuxun-Huobuxun lake fault.

Area (b) is the core site of the saline mud flat affected by the groundwater extraction and the construction of the infrastructures or buildings, these human activities may be the main factors that facilitate the dynamic evolution of area (b) [39,40]. As shown in Figure 12, the continuous subsidence caused by the extraction of underground brine is the outstanding characteristic in the drilling wells area around point T3. Similarly, the continuous subsidence appears in the Dabuxun Railway Station which is represented by R2. In the Dabuxun Railway Station, there is a subsidence funnel of 6 km from north to south and 4 km from east to west, and its accumulated subsidence has reached about 180 mm in the latest five years. Such a big subsidence funnel affects a large area around the station and has a great potential safety hazard, which needs our continuing concern in the future. Because of the over-exploitation and the weak foundation of saline soil, the extreme subsidence is the main characteristic in the areas of drilling wells and the Dabuxun Railway Station. Moreover, a significant subsidence occurs along the railway line in the southeastern part of Dabuxun Salt Lake. Such a dangerous deformation may be caused by the following reasons: (1) the rock salts (chlorine saline soil) characterized by high solubility and fast dissolution [40], would collapse caused by precipitation, surface runoffs and salt lake flooding in rainy seasons; (2) the confined water intrudes and dissolves the rock salt of the underground soil layer, thus many subsurface salt caves by water erosion come out and result in the collapse of the ground [41–43]. These factors would lead to serious security risks of the QTR and the Beijing-Tibet Expressway crossing the dry saline mud flat in the middle of the salt-lake.

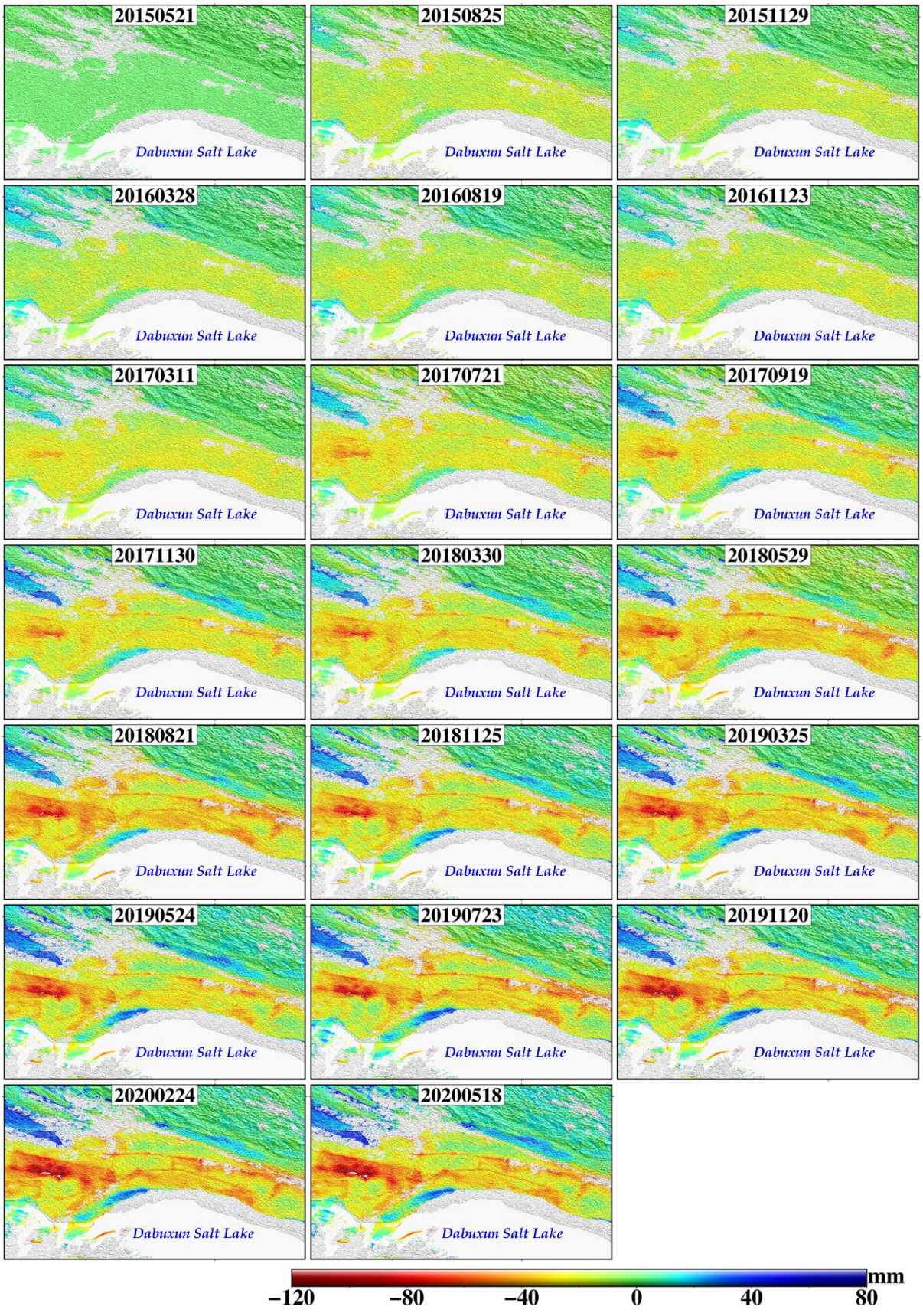

Figure 11. The accumulated deformation maps of area (a) from May, 2015 to May, 2020, each subplot is depicted with about 3 months' increments from the deformation results of TS-InSAR.

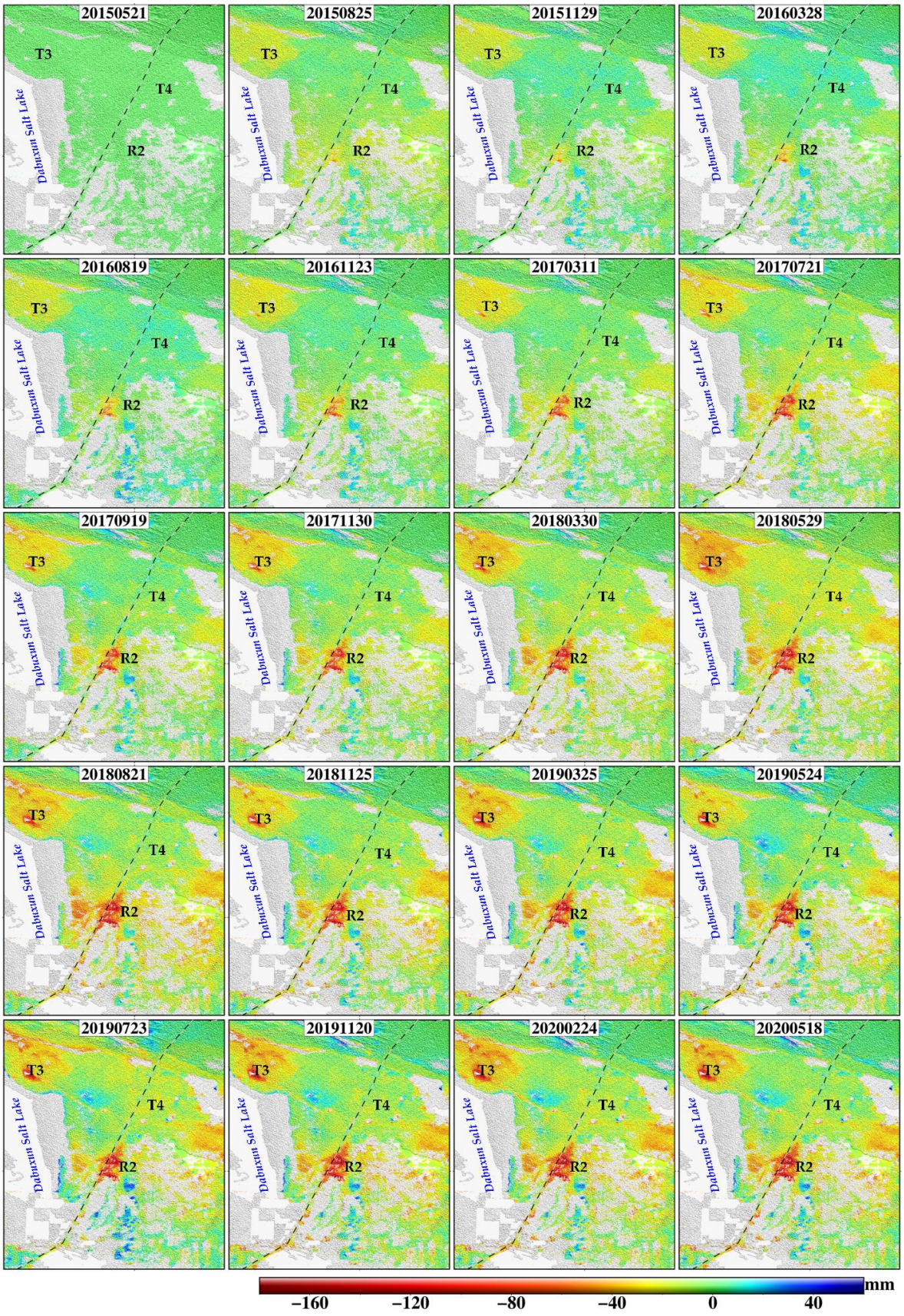

Figure 12. The accumulated deformation maps of area (b) from May, 2015 to May, 2020, each subplot is depicted with about 3 months' increments from the deformation results of TS-InSAR.

For further analyzing the complicated characteristics of the saline soil under different geological conditions or humanistic environment, we depicted the profiles of the deformation velocity in area (a) and area (b), respectively. As shown in Figure 13, we can know from the profile P1 of the deformation velocity that the DHLF is an obvious boundary of different deformation characteristics. Similarly, the profile P2 shows that there is an obvious boundary of deformation between sand flat and saline mud flat. In the sand flat, the deformation velocity of the selected CTs are close to 0 mm/a, while −4 mm/a to −37 mm/a in the saline mud flat. These different characteristics of deformation indicate that the foundation of the sand flat is more stable than that of the saline mud flat in the Qaidam Basin.

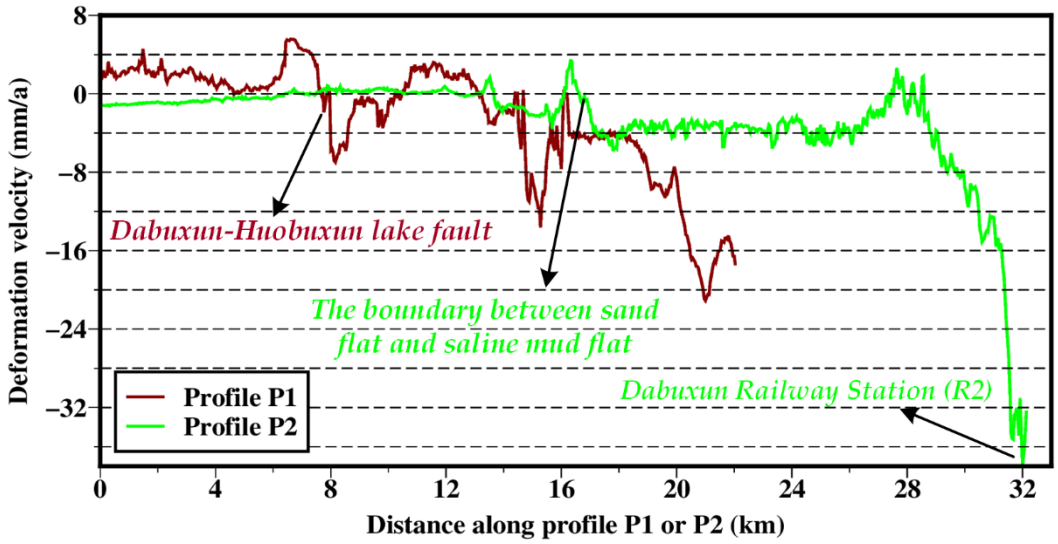

Figure 13. The profiles of the deformation velocity in area (a) and area (b), the dark red line indicates the profile P1 in area (a) and the green line indicates the profile P2 in area (b).

5.3. The Dynamic Evolution of Saline Soil

The deformation velocity map reflects the deformation characteristics of saline soil in a large scale, while the time-series deformations of the selected CTs help us understanding the dynamic evolution of saline soil furtherly and thoroughly. For a better analyzation of the dynamic evolution of saline soil in the Qaidam Basin, we selected six representative CTs from area (a) and area (b), whose coordinates are presented in Table 1. Each of the representative CTs reflects the deformation specificity of the saline soil under different environmental conditions. As shown in Figure 14, the apparent seasonal deformations are appeared at points T1, T2, T4 and R1. The maximum difference of the LOS deformation has reached 46 mm at point T1, and 43 mm at point T2 between the dry season and the rainy season in 2018. However, there is a general uplift at points T1 and T4, while a general subsidence at point T2. The seasonal fluctuations accompanied by a general linear deformation trend is a typical characteristic of the deformation in this saline-soil area. All the deformation characteristics of these CTs present the dynamic evolution process of the saline soil in the natural environment without the influences of human activities. However, points T3 and R2 affected by the artificial over-exploitation, and the accumulated subsidence has reached 150 mm from May 2015 to May 2020. The weak foundation of saline soil accelerates the continuous subsidence in the area of human activity.

Table 1. Latitude and longitude coordinates of the representative CTs.

CTs	Latitude (°N)	Longitude (°E)	CTs	Latitude (°N)	Longitude (°E)
T1	37.1335	95.1235	T4	37.0160	95.4260
T2	37.1082	95.2029	R1	37.2562	95.5599
T3	37.0418	95.2490	R2	36.9126	95.3671

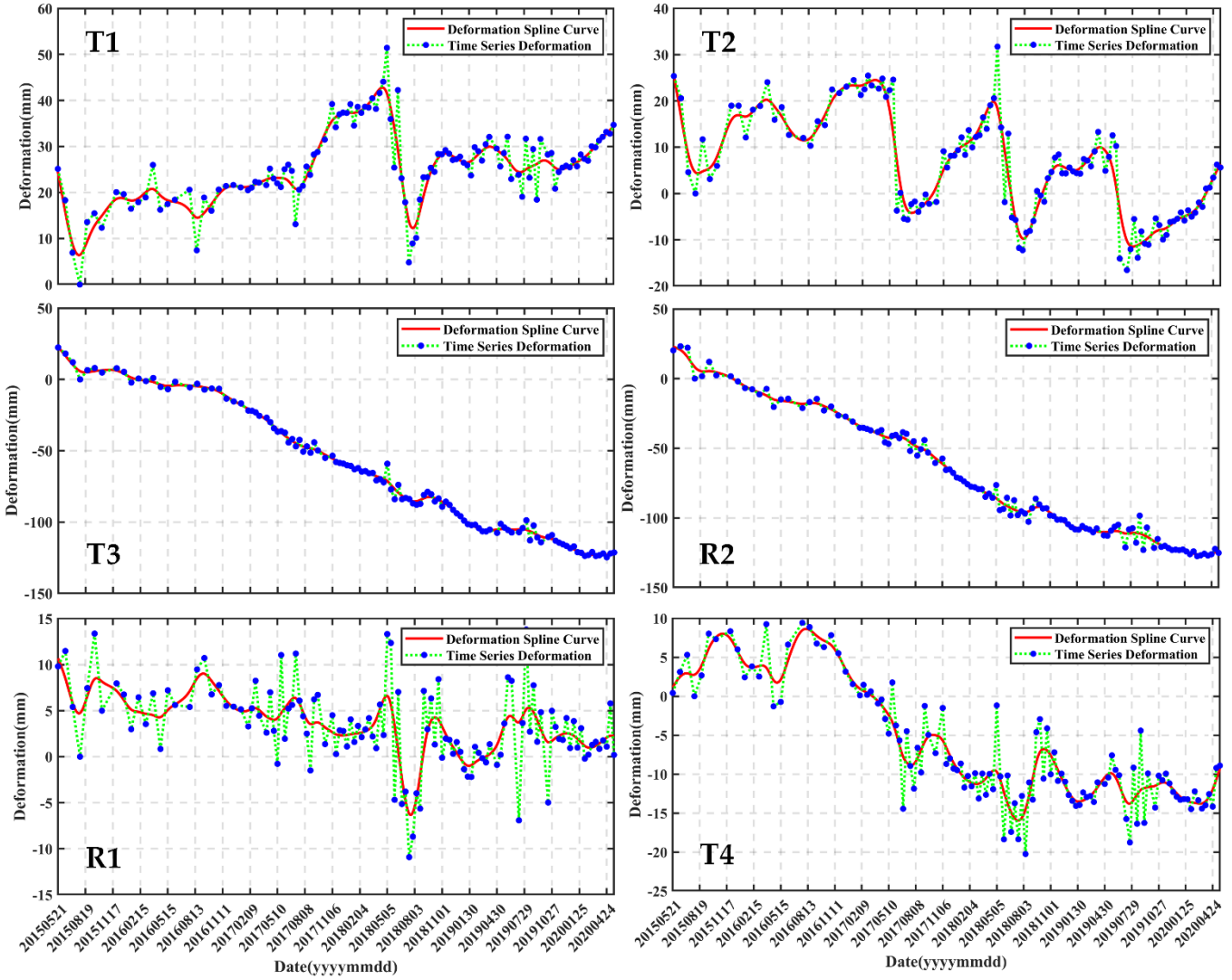

Figure 14. The time-series deformation of the representative CTs, the blue dots are the estimated results of the time-series deformation and the red line indicates the fitting result of the deformation spline curve.

6. Conclusions

In this paper we have presented an improved TS-InSAR approach especially refer to extracting ground deformation in the saline soil area with significant seasonal variations. The main contribution is to refine the high-coherence interferograms without the constraint of temporal baseline. With more high-quality and redundant interferograms in the same season, the accuracy and reliability of the deformation results are improved by the dense observations. Furthermore, the desired results in the same season limit the error propagation between different seasons and improve the accuracy and reliability of the final results after the adjustment calculation. Consequently, more high-quality and redundant

observations participated in the network inversion extend the adaptability and accuracy for ground deformation extraction in the saline soil area.

The deformation results derived from the improved TS-InSAR procedures are compared with those derived from the conventional SBAS-InSAR, and further analysis is conducted focusing on the differences of the deformation velocity in several representative areas. Two representative stable areas of S1 and S2 are selected to compare the accuracy and reliability in the space domain under such different processing procedures. The percentages of the small deformation velocity are increased from 33% to 79% in area S1 and 11% to 67% in area S2 under the procedures of the conventional SBAS-InSAR and the improved TS-InSAR, respectively. The comparison analysis indicates that the accuracy and reliability of the estimated deformation derived from the improved TS-InSAR are increased relative to those from the conventional SBAS-InSAR. Especially in the areas of weak foundation, i.e. salt desert, many complicated factors lead to significant seasonal fluctuations in the scattering characteristics and surface deformation. Moreover, the seasonal fluctuations decrease the quality of the estimated deformation, and even intensify the temporal decorrelation. However, the improved TS-InSAR method shows high adaptability and stability in saline soil area and obtains high-precision and reliable monitoring results. Related method and results can provide a reference for infrastructure construction and natural disaster prevention in such geological environment areas.

Author Contributions: Conceptualization, Guoxiang Liu and Rui Zhang; Data curation, Wei Xiang, Xiaowen Wang, Wenfei Mao, Bo Zhang, Yin Fu and Tingting Wu; Formal analysis, Wei Xiang; Methodology, Wei Xiang; Writing—original draft, Wei Xiang; Writing—review & editing, Guoxiang Liu, Rui Zhang and Wei Xiang. All authors have read and agreed to the published version of the manuscript.

Funding: This research was jointly funded by the National Natural Science Foundation of China (Grant No. 41771402, 41804009, 42071410); the National Key R&D Program of China (Grant No.2017YFB0502700); and the Sichuan Science and Technology Program (No. 2019ZDZX0042, 2020JDTD0003, 2020YJ0322).

Data Availability Statement: The climate data can be downloaded from the website: https://www.ncdc.noaa.gov/cdo-web/datasets/GHCND/stations/GHCND:CHM00052818/detail; the POD can be downloaded from the website: https://qc.sentinel1.eo.esa.int/aux_poeorb/?mission=S1A&validity_start_time=2015&validity_start_time=2015-12&validity_start_time=2015-12-25..2015-12-28; and the Sentinel-1A SAR images can be downloaded from the website: https://scihub.copernicus.eu/dhus/#/home.

Acknowledgments: The Sentinel-1A TOPS IW SLC SAR images and the POD data were provided by the Copernicus Sentinel-1 Mission of ESA. We also thank NASA for providing the SRTM DEM data.

Conflicts of Interest: The authors declare no conflict of interest.

References

1. Liu, G.X.; Ding, X.L.; Chen, Y.Q.; Li, Z.L.; Zheng, D.W. New and potential technology for observation of earth from space: Synthetic aperture radar interferometry. *Adv. Earth Sci.* **2000**, *15*, 734–740.
2. Massonnet, D.; Rossi, M.; Carmona, C.; Adragna, F.; Peltzer, G.; Feigl, K.; Rabaute, T. The displacement field of the landers earthquake mapped by radar interferometry. *Nature* **1993**, *364*, 138–142. [CrossRef]
3. Hooper, A.; Bekaert, D.; Spaans, K.; Arıkan, M. Recent advances in SAR interferometry time series analysis for measuring crustal deformation. *Tectonophysics* **2012**, *514–517*, 1–13. [CrossRef]
4. Massonnet, D.; Feigl, K.L. Radar interferometry and its application to changes in the earth's surface. *Rev. Geophys.* **1998**, *36*, 441–500. [CrossRef]
5. Bamler, R.; Hartl, P. Synthetic aperture radar interferometry. *Inv. Prob.* **1998**, *14*, R1–R54. [CrossRef]
6. Rosen, P.A.; Hensley, S.; Joughin, I.R.; Li, F.K.; Madsen, S.N.; Rodriguez, E.; Goldstein, R.M. Synthetic aperture radar interferometry. *Proc. IEEE* **2000**, *88*, 333–382. [CrossRef]
7. Buckley, S.M. Radar Interferometry Measurement of Land Subsidence. Ph.D. Thesis, University Texas, Austin, TX, USA, 2000.
8. Zebker, H.A.; Villasenor, J. Decorrelation in interferometric radar echoes. *IEEE Trans. Geosci. Remote Sens.* **1992**, *30*, 950–959. [CrossRef]

9. Ferretti, A.; Prati, C.; Rocca, F. Nonlinear subsidence rate estimation using permanent scatterers in differential SAR interferometry. *IEEE Trans. Geosci. Remote Sens.* **2000**, *38*, 2202–2212. [CrossRef]
10. Farolfi, G.; Piombino, A.; Catani, F. Fusion of GNSS and Satellite Radar Interferometry: Determination of 3D Fine-Scale Map of Present-Day Surface Displacements in Italy as Expressions of Geodynamic Processes. *Remote Sens.* **2019**, *11*, 394. [CrossRef]
11. Colesanti, C.; Ferretti, A.; Prati, C.; Rocca, F. Monitoring landslides and tectonic motions with the Permanent Scatterers Technique. *Eng. Geol.* **2003**, *68*, 3–14. [CrossRef]
12. Ansari, H.; Zan, F.D.; Bamler, R. Sequential estimator: Toward efficient InSAR time series analysis. *IEEE Trans. Geosci. Remote Sens.* **2017**, *55*, 5637–5652. [CrossRef]
13. Schmidt, D.A.; Bürgmann, R. Time-dependent land uplift and subsidence in the Santa Clara valley, California, from a large interferometric synthetic aperture radar data set. *J. Geophys. Res. Solid Earth* **2003**, *108*, B9. [CrossRef]
14. Hooper, A. A multi-temporal InSAR method incorporating both persistent scatterer and small baseline approaches. *Geophys. Res. Lett.* **2008**, *35*, 1–5. [CrossRef]
15. Liu, G.X.; Buckley, S.M.; Ding, X.L.; Chen, Q.; Luo, X.J. Estimating spatiotemporal ground deformation with improved persistent scatterer radar interferometry. *IEEE Trans. Geosci. Remote Sens.* **2009**, *47*, 3209–3219. [CrossRef]
16. Liu, G.X.; Luo, X.J.; Chen, Q.; Huang, D.F.; Ding, X.L. Detecting land subsidence in Shanghai by PS-networking SAR interferometry. *Sensors* **2008**, *8*, 4725–4741. [CrossRef] [PubMed]
17. Liu, G.X.; Jia, H.G.; Zhang, R.; Zhang, H.X.; Jia, H.L.; Yu, B.; Sang, M.Z. Exploration of subsidence estimation by persistent scatterer InSAR on time series of high resolution TerraSAR-X images. *IEEE J. Sel. Top. Appl. Earth Obs. Remote Sens.* **2011**, *4*, 159–169. [CrossRef]
18. Berardino, P.; Fornaro, G.; Lanari, R.; Sansosti, E. A new algorithm for surface deformation monitoring based on small baseline differential SAR interferograms. *IEEE Trans. Geosci. Remote Sens.* **2002**, *40*, 2375–2383. [CrossRef]
19. Lanari, R.; Mora, O.; Manunta, M.; Mallorqui, J.J.; Berardino, P.; Sansosti, E. A small-baseline approach for investigating deformations on full-resolution differential SAR interferograms. *IEEE Trans. Geosci. Remote Sens.* **2004**, *42*, 1377–1386. [CrossRef]
20. Ferretti, A.; Fumagalli, A.; Novali, F.; Prati, C.; Rocca, F.; Rucci, A. A new algorithm for processing interferometric data-stacks: SqueeSAR. *IEEE Trans. Geosci. Remote Sens.* **2011**, *49*, 3460–3470. [CrossRef]
21. Perissin, D.; Wang, T. Repeat-Pass SAR Interferometry with Partially Coherent Targets. *IEEE Trans. Geoence Remote Sens.* **2011**, *50*, 271–280. [CrossRef]
22. Tizzani, P.; Berardino, P.; Casu, F.; Euillades, P.; Manzo, M.; Ricciardi, G.P.; Zeni, G.; Lanari, R. Surface deformation of Long Valley Caldera and Mono Basin, California, investigated with the SBAS-InSAR approach. *Remote Sens. Environ.* **2007**, *108*, 277–289. [CrossRef]
23. Casu, F.; Manzo, M.; Pepe, A.; Lanari, R. SBAS-DInSAR analysis of very extended areas: First results on a 60000-km2 test site. *IEEE Geosci. Remote Sens. Lett.* **2008**, *5*, 438–442. [CrossRef]
24. Barbouchi, M.; Abdelfattah, R.; Chokmani, K.; Ben Aissa, N.; Lhissou, R.; El Harti, A. Soil salinity characterization using polarimetric insar coherence: Case studies in tunisia and morocco. *IEEE J. Sel. Top. Appl. Earth Obs. Remote Sens.* **2015**, *8*, 3823–3832. [CrossRef]
25. Francesco, D.Z.; Zonno, M.; Paco, L.D. Phase Inconsistencies and Multiple Scattering in SAR Interferometry. *IEEE Trans. Geoence Remote Sens.* **2015**, *53*, 6608–6616.
26. Jiang, M. Sentinel-1 TOPS co-registration over low-coherence areas and its application to velocity estimation using the all pairs shortest path algorithm. *J. Geod.* **2020**, *94*, 1–15. [CrossRef]
27. Fattahi, H.; Agram, P.; Simons, M. A network-based enhanced spectral diversity approach for TOPS time-series analysis. *IEEE Trans. Geosci. Remote Sens.* **2016**, *55*, 777–786. [CrossRef]
28. Gao, B.L.; Wang, J.C.; Li, Y. Research on the salt soluble disasters of saline lake subgrade along the Qinghai-Tibet railway in Chaerhan Salt Lake region. *J. Railw. Eng. Soc.* **2015**, *32*, 6–11. (In Chinese)
29. Liu, G.X.; Jia, H.G.; Nie, Y.; Li, T.; Zhang, R.; Yu, B.; Li, Z.L. Detecting subsidence in coastal areas by ultrashort-baseline tcpinsar on the time series of high-resolution terrasar-x images. *IEEE Trans. Geoence Remote Sens.* **2014**, *52*, 1911–1923. [CrossRef]
30. Zhang, Y.J.; Fattahi, H.; Amelung, F. Small baseline InSAR time series analysis: Unwrapping error correction and noise reduction. *Comput. Geosci.* **2019**, *133*, 104331.
31. Pepe, A.; Lanari, R. On the extension of the minimum cost flow algorithm for phase unwrapping of multitemporal differential SAR interferograms. *IEEE Trans. Geosci. Remote Sens.* **2006**, *44*, 2374–2383. [CrossRef]
32. Costantini, M. A novel phase unwrapping method based on network programming. *IEEE Trans. Geoence Remote Sens.* **1997**, *36*, 813–821. [CrossRef]
33. Ansari, H.; Zan, F.D.; Bamler, R. Efficient phase estimation for interferogram stacks. *IEEE Trans. Geosci. Remote Sens.* **2018**, *56*, 4109–4125. [CrossRef]
34. Samiei-Esfahany, S.; Martins, J.E.; Leijen, F.V.; Hanssen, R.F. Phase estimation for distributed scatterers in InSAR stacks using integer least squares estimation. *IEEE Trans. Geosci. Remote Sens.* **2016**, *54*, 5671–5687. [CrossRef]
35. Seymour, M.S.; Cumming, I.G. Maximum likelihood estimation for SAR interferometry. *Geosci. Remote Sens. Symp. Igarss* **1994**, *94*, 8–12.
36. Lowenstein, T.K.; Risacher, F. Closed basin brine evolution and the influence of Ca-Cl inflow waters: Death Valley and Bristol Dry Lake California, Qaidam Basin, China, and Salar de Atacama, Chile. *Aquat. Geochem.* **2009**, *15*, 71–94. [CrossRef]

37. Wei, H.C.; Fan, Q.S.; An, F.Y.; Shan, F.S.; Ma, H.Z.; Yuan, Q.; Qin, Z.J. Chemical elements in core sediments of the Qarhan Salt Lake and palaeoclimate evolution during 94–9 ka. *Acta Geosci. Sin.* **2016**, *2*, 193–203. (In Chinese)
38. Zhu, Y.Z.; Li, Z.Y.; Wu, B.L.; Wang, M.L. The Formation of the Qarhan Saline Lakes as Viewed from the Neotectonic Movement. *Acta Geol. Sin.* **1990**, *64*, 13–21. (In Chinese)
39. Yu, S.S.; Tan, H.B.; Liu, X.Q.; Cao, G.C. *Sustainable Utilization of Qarhan Salt Lake Resources*; Science Press: Beijing, China, 2009. (In Chinese)
40. Yang, H.R.; Jiang, F.Q.; Wang, X.; Zhang, J.D. Characteristics of rock salt and salt-dissolution engineering geology and subgrade construction in Chaerhan Salt Lake along Qinghai-Tibet railway. *J. Railw. Eng. Soc.* **2005**, *000(0z1)*, 373–378. (In Chinese)
41. Zhang, Z.C.; Wang, S.Z. Long-term monitoring of subgrade stability of the Qinghai-Tibet railway in the Charhan playa region. *Int. J. Rock Mech. Min. Ences Geomech. Abstr.* **1988**, *25*, 241.
42. Sun, J.L.; Wang, S.Z.; Bai, L.T.; Zhang, Z.C. An analysis of the stability of railway in Chaerhan Saline Lake area. *J. Beijing Univ. Technol.* **1980**, *3*, 52–65. (In Chinese)
43. Yu, C.; Penna, N.T.; Li, Z.H. Generation of real-time mode high-resolution water vapor fields from GPS observations. *J. Geophys. Res. Atmos.* **2017**, *122*, 2008–2025. [CrossRef]
44. Yu, C.; Li, Z.H.; Penna, N.T. Interferometric synthetic aperture radar atmospheric correction using a GPS-based iterative tropospheric decomposition model. *Remote Sens. Environ.* **2018**, *204*, 109–121. [CrossRef]
45. Wang, C.N.; Guo, X.H.; Ma, M.Z.; Li, J.-D. Ore-forming Geological Background of K-Mg Salt in Qarhan Salt Lake. *Northwestern Geol.* **2008**, *41*, 97–106.